ACS APPLIED NANO MATERIALS

www.acsanm.org Article

Thick-Shell CdSe/ZnS/CdZnS/ZnS Core/Shell Quantum Dots for Quantitative Immunoassays

Yanbing Lv, Yucheng Yuan, Ning Hu, Na Jin, Dangdang Xu,* Ruili Wu, Huaibin Shen, Ou Chen,* and Lin Song Li*

Cite This: *ACS Appl. Nano Mater.* 2021, 4, 2855−2865 Read Online

ACCESS | Metrics & More | Article Recommendations | Supporting Information

ABSTRACT: Colloidal quantum dots (QDs) have been broadly applied as fluorescent labeling materials in the fields of bio-imaging, sensing, and detection, in which the optical performances and stability of the utilized QDs are vital. Despite significant efforts in developing such materials, it is still challenging to fabricate QDs with high photoluminescence quantum yields (PL QYs) while concurrently possessing high particle and optical stabilities, limiting the further development of QD-based biological labeling and detection techniques. Herein, we report a synthesis of giant CdSe/ZnS/CdZnS/ZnS core/shell QDs with an ultrathick shell (~36 monolayers) and high PL QYs (>80%). We further employ the as-synthesized QDs for C-reactive protein detection, which reach nearly a 3-fold enhancement in detection sensitivity (~0.41 ng/mL) and a 2-fold increase in shelf life, in comparison to the traditional thick-shell QDs (*i.e.*, CdSe/CdS/ZnS core/shell QDs) or commercially available core/shell QDs. We postulate that the performance improvements in protein detection are due to the use of the developed core/shell QDs with high particle stability and PL QYs and large surface area (facilitating surface antibody coupling). Our study demonstrates the viability of applying high-quality core/shell QDs for protein detection with high sensitivity and accuracy.

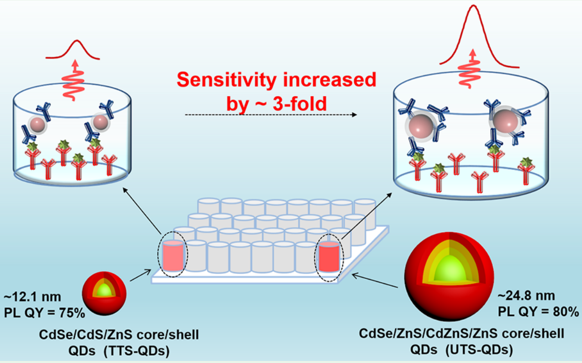

KEYWORDS: *ultrathick-shell QDs, core/shell QDs, QD-based fluorescence-linked assay (QDs-FLISA), C-reactive protein, quantitative immunoassay*

Downloaded via BROWN UNIV on April 30, 2021 at 16:48:53 (UTC).
See https://pubs.acs.org/sharingguidelines for options on how to legitimately share published articles.

1. INTRODUCTION

Colloidal quantum dots (QDs) with high photoluminescence quantum yields (PL QYs), high resistance to photobleaching and chemical and physical degradations, and excellent biocompatibility have proven to be unique optical materials in various bio-related applications,[1−4] including visualization of cellular processes,[5−8] *in vitro* and *in vivo* labeling and imaging,[9−12] targeted drug delivery,[13,14] gene sequencing,[15,16] and quantitative bio-molecule detection.[17,18] Particularly, colloidal QDs have been considered as ideal fluorescent labeling materials for high-sensitivity protein detections in clinical diagnosis.[19] Since Goldman and co-workers' pioneer work on the successful application of QDs to fluoroimmunoassays (*i.e.*, QD-based fluorescence-linked immunosorbent assay, QDs-FLISA),[20] QDs with various structures and compositions have been subsequently applied to *in vitro* diagnostics (IVD).[21−23] However, one of the long-lasting limitations for applying QDs to IVD is their fluorescence instability in physiological environments, which reduces detection sensitivity and shortens the shelf time, hence inhibiting accurate quantitative detection in chemiluminescence immunoassay, biological labeling, sensing, and detection.[24,25]

When applying QDs with antibody conjugation to the field of biological detection, it is imperative to fabricate the QDs with high particle and optical stabilities and concurrently good coupling capacity of antibodies.[26] Although traditional QDs in organic solution exhibit rather high PL QYs (>80%), they often experience a drastic QY loss upon being transferred to an aqueous solution due to their non-ideal optical stability (*e.g.*, PL QYs decrease due to insufficient exciton confinement and/or particle surface protection).[27−29] In addition, traditional QDs with small particle sizes (2−10 nm in diameter) can only provide limited surface areas of individual QDs for bio-molecule coupling, which further limits their performances in bio-related labeling and detection applications, such as in QDs-FLISA.[30] Those challenges can be effectively overcome by designing and synthesizing core/shell QDs with thick shells (>10 monolayers, MLs).[31,32] The optical properties of QDs

Received: December 31, 2020
Accepted: February 26, 2021
Published: March 10, 2021

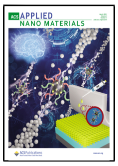

© 2021 American Chemical Society

Scheme 1. Schematic Illustration of the Preparation of QDs and the QDs-FLISA Procedure

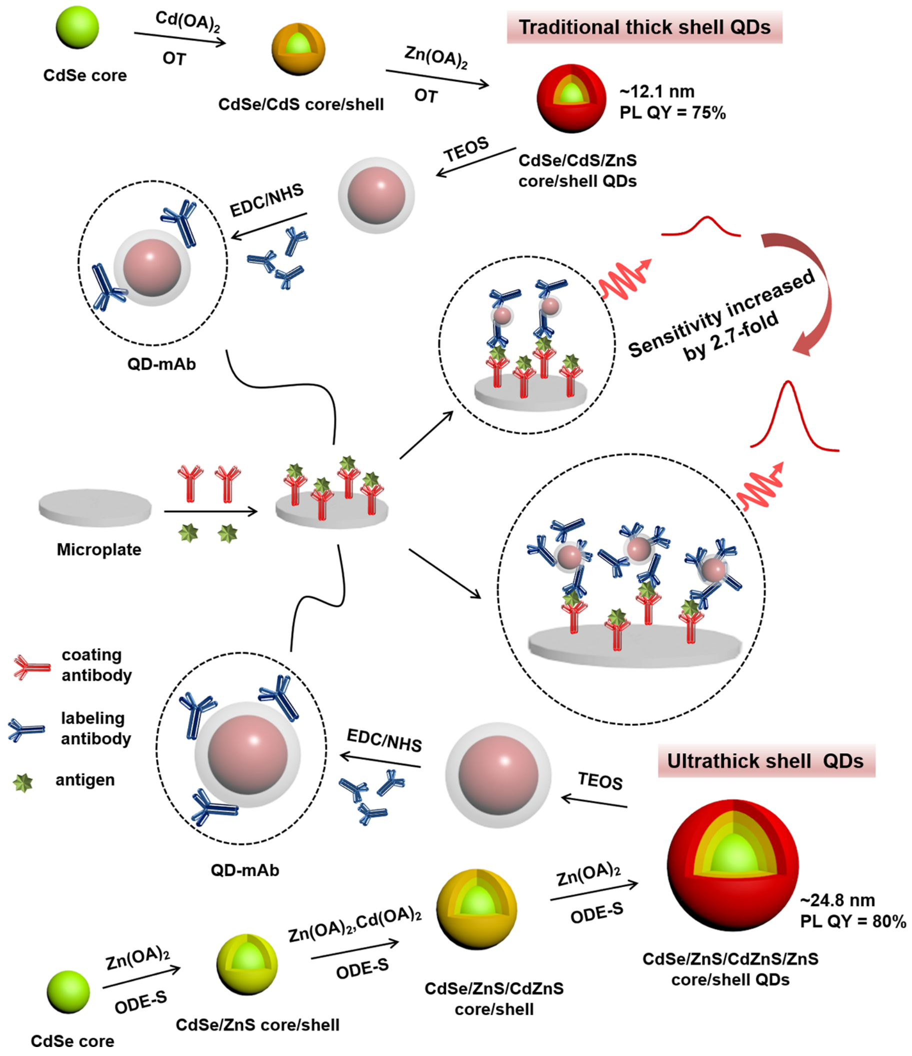

can be improved with thick-shell coating, including enhancing PL QY, suppressing blinking and Auger recombination, improving stability, *etc.*[33−36] For example, Bawendi and co-workers reported a synthesis of high-quality CdSe/CdS core/shell QDs (PL QYs up to 97%) by a slow growth of CdS shell using octanethiol as the sulfur precursor.[34] Besides, large QDs can adequately provide larger surface areas for further bio-modifications, which allows for better bio-molecule detection efficiency and accuracy.[37] A common way to obtain large-size fluorescent probes is to prepare QD-modified nano/micro-spheres. For example, fluorescent nanospheres coated with multiple QDs were prepared by Pang's group for quantitative detection of C-reactive protein (CRP) with a detection sensitivity of 3.89 ng/mL.[38] Later, Li *et al.* prepared high-quality QD nanobeads with a large particle surface area that allows coupling sufficient antibodies and improving detection sensitivity.[37] In this regard, it is valuable to develop a new synthetic route of thick-shell core/shell QDs with large and uniform particle sizes, superior optical outputs, and improved particle and optical stabilities, especially for high-sensitivity bio-detections of specific proteins.

Herein, we report a new design and synthesis of ultrathick-shell (UTS) CdSe/ZnS/CdZnS/ZnS core/shell QDs with superior optical properties at both single-dot and ensemble levels (Scheme 1). A large size of the UTS-QDs (particle diameter of >24 nm) can be achieved by a long-term shell growth and the introduction of an alloy bridging layer at a high reaction temperature (≥310 °C). The PL QY of the resultant UTS-QDs reaches above 80%, and the single-dot blinking behavior is greatly suppressed. We have successfully transferred the UTS-QDs into an aqueous solution through silica encapsulation by a reverse microemulsion method. After conjugating with sufficient CRP antibody, we show that the resulting UTS-QD@SiO$_2$−antibody probes can be applied to quantitatively detect CRP antigens using a QDs-FLISA. We observe a nearly 3-fold enhancement in detection sensitivity (~0.41 ng/mL) and a 2-fold increase in lifetime of QDs-FLISA (14 days at 45 °C) in comparison to the traditional thick-shell QDs (TTS-QDs, *i.e.*, CdSe/CdS/ZnS core/shell QDs) or other commercially available core/shell QDs. We attribute these major advances of the UTS-QDs with excellent optical properties and stabilities to UTS engineering, providing an excellent platform for future applications of high-sensitive bio-molecule detections in IVD and beyond.

2. RESULTS AND DISCUSSION

Synthesizing QDs with high PL QYs and large particle sizes, thus a larger surface area of individual QDs, is of importance

https://dx.doi.org/10.1021/acsanm.0c03483
ACS Appl. Nano Mater. 2021, 4, 2855−2865

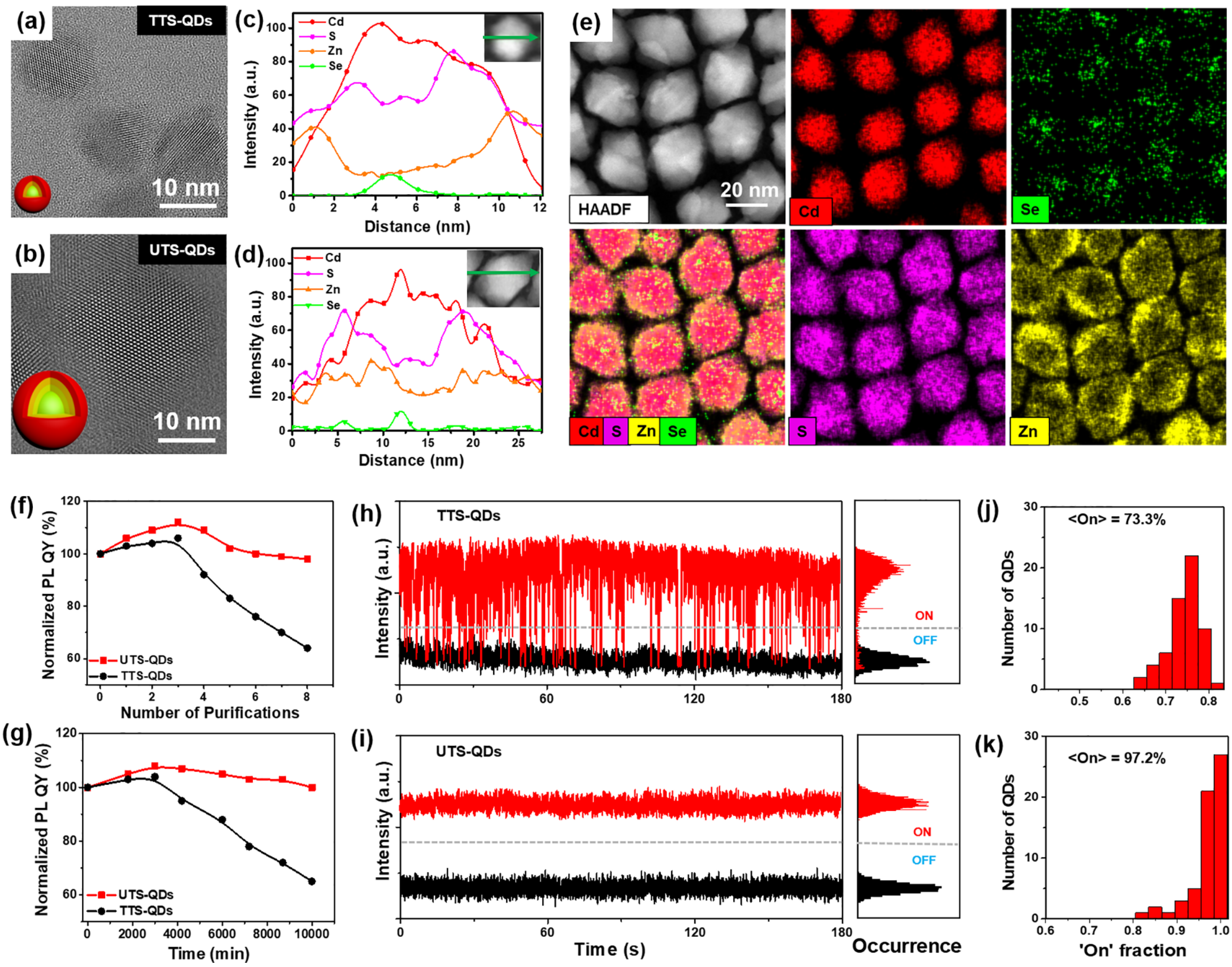

Figure 1. High-resolution transmission electron microscopy (HR-TEM) images of TTS-QDs (a) and UTS-QDs (b) (insets are the schematic illustration of TTS-QDs and UTS-QDs). Elemental profiles of Cd, Zn, S, and Se from a typical QD as indicated by the green arrow in the dark-field scanning transmission electron microscopy (STEM) image (inset) of TTS-QDs (c) and UTS-QDs (d). STEM image of UTS-QDs and energy-dispersive spectroscopy elemental maps of Cd, Se, S, and Zn in the same UTS-QDs array (e). Evolution of the relative PL stability of TTS-QDs (black line) and UTS-QDs (red line) (f). Photochemical stability of TTS-QDs (black line) and UTS-QDs (red line) in hexane solution (g). Blinking behavior of a single TTS-QD (h) and UTS-QD (i) for 180 s, with a binning time of 20 ms. The red and black traces are the PL intensities of a single QD and the corrected background noise intensities, respectively. Correspondingly, the distribution of the PL intensity is plotted on the right side of each trace. Laser at 458 nm with an excitation power of 35 mW was selected to characterize this property. Histograms of the blinking "on" time fraction for TTS-QDs (j) and UTS-QDs (k).

for realizing high-sensitivity biological detection. To meet the requirements, we have developed a new synthetic scheme for fabricating UTS CdSe/2ZnS/30CdZnS/4ZnS core/shell QDs (the numerical value represents the number of shell ML, which is defined as a single layer of cationic and anionic deposition[39]) using sulfur-octadecene (S-ODE) and zinc-oleate ($Zn(OA)_2$) as shell precursors (see the Experimental Section in the Supporting Information for synthetic details and Figure S1 for the band gap alignment diagram). We optimized the thickness of the inner ZnS shell layer based on the optical performance (*e.g.*, PL QYs) of the final sample. In addition, the intermediate CdZnS shell (growth at 310 °C) can provide a cushion layer (reducing the lattice strains at the core/shell and shell/shell interfaces) and allow a smooth reach of the final UTS-QDs. These UTS-QDs were designed to effectively prevent the delocalization of the exciton wave function,[40,41] thus minimizing the impact on the optical properties of the QDs from surrounding environments, which were crucial for the subsequent CRP detection using QDs-FLISA application discussed later.

For comparison, we also synthesized traditional thick-shell CdSe/10CdS/4ZnS QDs (TTS-QDs) following our previously published procedure (see Figure S1 for the band gap alignment diagram).[42,43] The TTS-QDs exhibited a PL peak centered at 621 nm and a high PL QY of 75% (Figure S2). A zinc-blende (ZB) crystal structure of the TTS-QDs was characterized based on the X-ray diffraction (XRD) pattern with a high crystallinity as proven by high-resolution transmission electron microscopy (HR-TEM) measurements (Figure 1a). Energy-dispersive spectroscopy (EDS) elemental mapping of the four respective elements, *i.e.*, Cd, Se, S, and Zn, for the TTS-QDs is shown in Figure S5, and the corresponding elemental profiles of Cd, S, Zn, and Se of a typical sample are shown in Figure 1c. It was found that the Cd element mainly appeared in the core and inner shell regions, while the Se element was mainly detected in the core region (Figure 1c and Figure S5c). In stark contrast, the Zn element dominantly distributed in the outer layer shell region, indicating no diffusion into the inner core.[32] The extension of Zn element distribution along the radial direction was measured to be around 1.3 nm, in line with the thickness of the ZnS shell layer (approximately four MLs).

During the synthesis of UTS-QDs, the PL peak first experienced a gradual red shift to 613 nm with inner ZnS shell coating, and then a blue shift down to 606 nm was observed after coating with the CdZnS alloy shell and the outmost ZnS shell (Figure S3a). Comparing with the TTS-QDs, the smaller red shift of the PL peak for the UTS-QDs was due to the increased quantum confinement effects induced by Zn-dominated shell layers.[44] The first exciton absorption peak of the UTS-QDs was gradually flattened and became less noticeable during shell growth (Figure S3a). In contrast, the absorption of the lower wavelength (higher energy) part of the absorption spectrum was enhanced (Figure S3a). During the shell growth, full width at half-maximum (FWHM) of the PL peak increased from 26 to 36 nm (Figure S3c). The overall PL QYs reached above 80% during the shelling process, with the maximum value of 97% at a shell thickness of 12 MLs (2 MLs of ZnS and 10 MLs of CdZnS) (Figure S3d). Time-resolved PL decay lifetime measurements showed a single exponential decay curve with a lifetime of ∼16.8 ns at a shell thickness of 12 MLs (Figure S3e). The fluorescence lifetime of QDs gradually increased with the increase in shell thickness,[45] and it appeared double-exponential decay when the shell thickness increased to 36 MLs (CdSe/2ZnS/30CdZnS/4ZnS), including a fast decay (τ_1 = 24.7 ns) and a slow decay (τ_2 = 93.37 ns) component of PL lifetime. High crystallinity of the synthesized UTS-QDs can be well confirmed by the HR-TEM image (Figure 1b). Interestingly, the crystal structure of the QDs altered from a ZB to wurtzite (WZ) phase during the CdZnS alloy shelling process. The (111) characteristic peaks of the ZB CdSe core were gradually replaced by the (100), (002), and (101) peaks (Figure 2b). Meanwhile, two fingerprint diffraction peaks of (102) and (103) of WZ crystal phase appeared (Figure 2b). Similar ZB-to-WZ crystal phase transition was observed with the presence of fatty-amine in the solution.[46] In addition, the WZ crystal phase is thermodynamically favored at high reaction temperature (above 280 °C) during the shell growth in our study.[7,36,47,48]

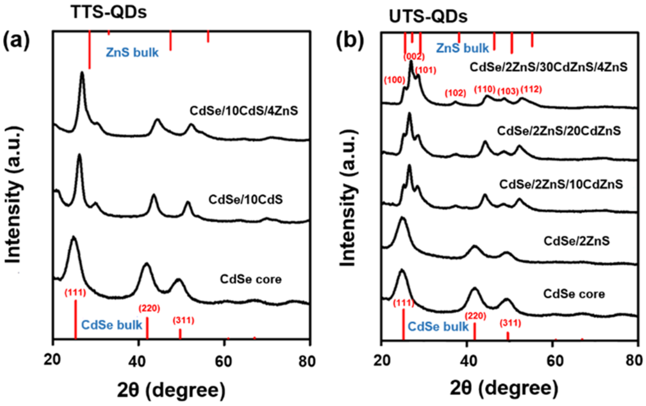

Figure 2. XRD patterns of CdSe core and TTS-QDs (a) and CdSe core and UTS-QDs (b).

The atomically resolved aberration-corrected high-angle annular dark-field scanning transmission electron microscopy (HAADF-STEM) measurements proved that the UTS-QDs possess well-defined core/shell structures, and elemental distribution profiles of Cd, Se, S, and Zn for a typical core/shell QD are shown in Figure 1d. The elemental distributions shown in Figure 1e clearly show that Se is mainly in the core, Zn disperses in the shells from inside to outside, and Cd can be mostly found in the core and intermediate layers, consistent with the data displayed in Figure 1d, suggesting the formation of a gradient alloy shell layer during the high-temperature shell growth (see details in Figure S4 in the Supporting Information).

It is known that the optical properties of QDs are highly sensitive to the quality of the QD surface and the surrounding solution environment.[49−51] To test the optical stability of the UTS-QDs, the PL QY evolution was monitored during the purification process. It was found that the PL QY of the UTS-QDs showed minimal variations during eight rounds of purification process using chloroform/acetone (see purification details in the Experimental Section and Figure 1f). In stark contrast, the PL QY of TTS-QDs experienced a significant drop after only four rounds of purification following the same purification procedure (Figure 1f). The PL stability of the UTS-QDs was also examined using the purified QDs (approximately eight rounds of purification) under 365 nm UV light illumination over a long period of time (∼7 days). As shown in Figure 1g, the UTS-QDs exhibited nearly no change in PL intensity, signifying a superior optical stability of the sample. In contrast, the PL QY of the TTS-QDs started to decrease after 2-day illumination and dropped to around 64% of the initial value after 7-day continuous excitation (Figure 1g). Similar optical stabilities under UV illumination were observed for four different commercially available core/shell QDs (Figure S12).

To further evaluate the optical property of the obtained UTS-QDs at the single-dot level, we characterized the PL blinking behavior of the UTS-QDs at the single-particle level and compared the results with that of the TTS-QDs (Figure 1h−k). PL blinking or fluorescence intermittence is a characteristic phenomenon of random switching between ON (bright) and OFF (dark) states of the emitter under continuous optical excitation, which can be well examined by recording the single-QD fluorescence traces within a certain period of time.[52,53] Two representative blinking traces for the TTS-QDs and UTS-QDs are shown in Figure 1h,i, respectively. An average "on" time fraction was extracted from the blinking traces from 60 different QDs for each measured sample.[54] An average "on" time fraction of TTS-QDs was determined to be ∼73.3% (Figure 1j), while the UTS-QDs exhibited a significantly suppressed blinking behavior with an average "on" time fraction reaching 97.2% (Figure 1k). The superior PL stability and suppressed blinking behavior of the UTS-QDs can be, respectively, attributed to the thick-shell protection and suppressed Auger recombination.[33,35,55]

One of the most formidable tasks of using QDs for biological applications is to retain high PL QYs of the QDs after transferring them from the organic phase to an aqueous solution. To make our UTS-QDs water-soluble and biocompatible, we have encapsulated the QDs with a transparent silica layer through a reverse microemulsion procedure (see the Experimental Section in the Supporting Information).[45] Low-magnification TEM images revealed that both types of hexane-

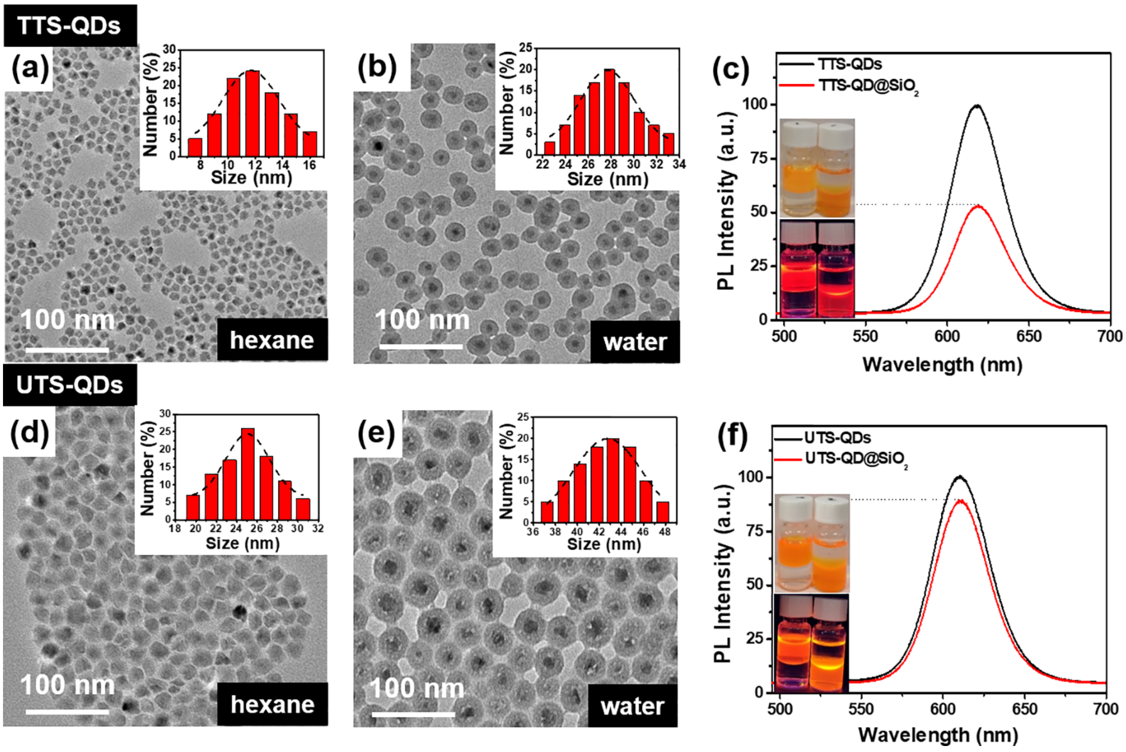

Figure 3. TEM images of the hydrophobic TTS-QDs (a) and UTS-QDs (d) in hexane and the corresponding TTS-QD@SiO$_2$ (b) and UTS-QD@SiO$_2$ (e) in water. Insets: size distribution histograms. PL spectra of hydrophobic TTS-QDs and UTS-QDs (black lines) and corresponding aqueous QD@SiO$_2$ (red lines) (c and f). Insets: photographs of hydrophobic QDs (left) and corresponding aqueous QDs (right) under room light (top pictures) and 365 nm ultraviolet light (bottom pictures) (upper phase is hexane; bottom phase is H$_2$O).

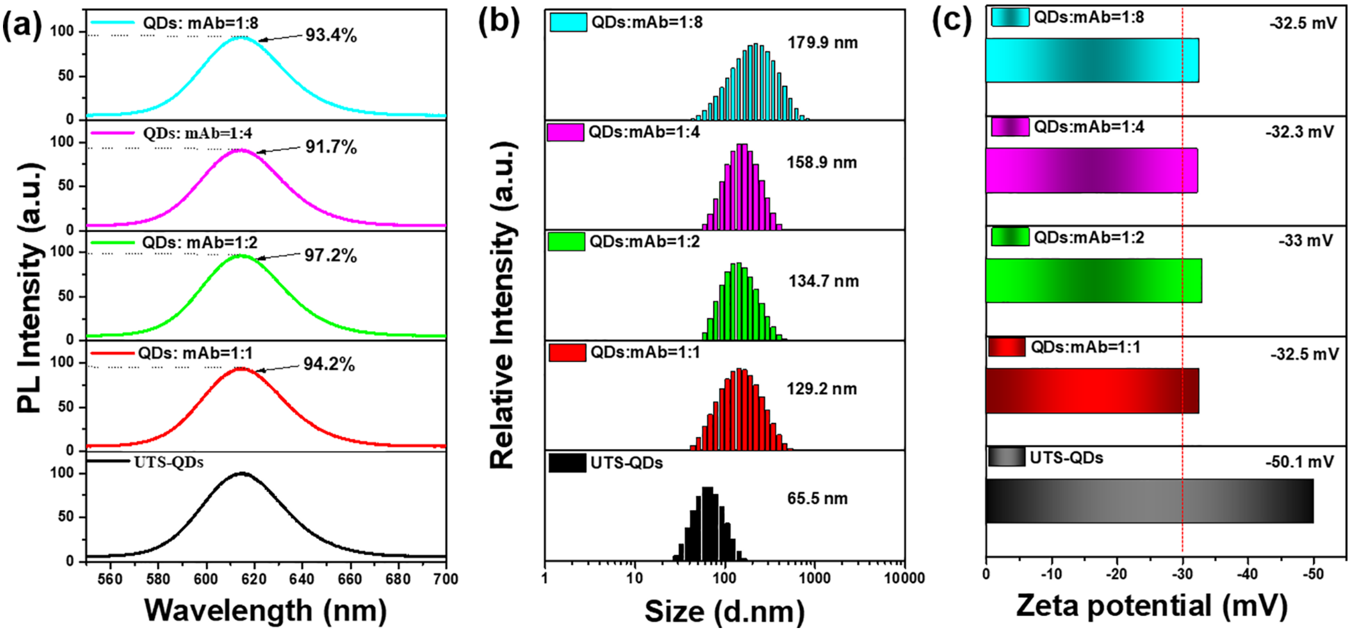

Figure 4. PL spectra (a), dynamic light scattering analysis (b), and zeta potentials (c) of UTS-QD@SiO$_2$ with different concentrations of CRP2 antibodies.

dispersed QD samples (*i.e.*, TTS-QDs and UTS-QDs) exhibited good particle size and morphology uniformity (TTS-QDs, 12.1 ± 1.3 nm; UTS-QDs, 24.8 ± 1.6 nm) (Figure 3a,d). Upon silica encapsulation, the average particle diameters increased to 27.2 ± 1.5 nm and 42.3 ± 2.3 nm for the TTS-QDs and UTS-QDs, respectively (Figure 3b,e), indicating similar silica coating thicknesses for these two samples (7.6 nm for TTS-QDs and 8.8 nm for UTS-QDs). While the TTS-QD@SiO$_2$ particles showed a 48% PL intensity decrease after transferring to the aqueous phase, the UTS-QD@SiO$_2$ particles exhibited a much improved resistance to the organic-to-aqueous phase transfer procedure,[56,57] showing only a PL intensity decrease of ~12% (Figure 3c,f); the final PL QYs of these TTS-QDs and UTS-QDs were 58% and 72%,

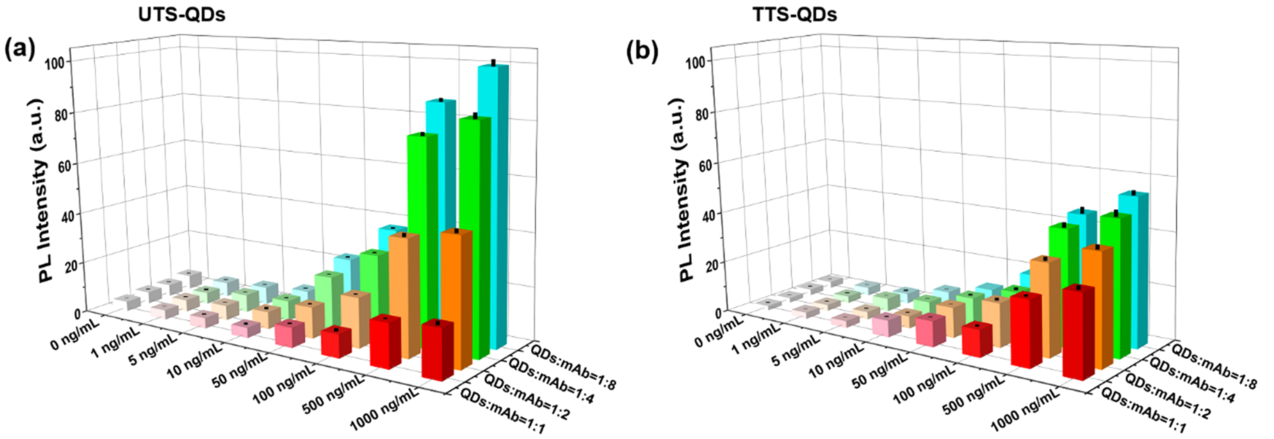

Figure 5. PL intensity of UTS-QD@SiO_2 (a) and TTS-QD@SiO_2 (b) with different ratios of antibodies: QD:mAb = 1:1, QD:mAb = 1:2, QD:mAb = 1:4, and QD:mAb = 1:8 from the QDs-FLISA method for CRP antigen detection.

respectively. In addition, the PL peak position of the UTS-QDs was marginally affected by silica encapsulation, demonstrating their excellent PL output stability upon solvent environment variation (Figure 3f).

We next examined the pH, thermal, and photostabilities of the obtained water-soluble QD@SiO_2, which are the key requirements for applications such as QDs-FLISA. While the PL intensity of TTS-QD@SiO_2 was only stable in a narrow pH window of 9−10, UTS-QD@SiO_2 showed an excellent stability in a much wider pH range of 3−14, with less than 20% PL intensity loss (Figure S6a). Next, we have monitored the thermal and photostabilities of these QDs in water for 7 consecutive days. In contrast to the TTS-QD@SiO_2 case in which the PL intensity dropped drastically upon heating to 80 °C, the PL intensity of UTS-QD@SiO_2 showed a much less decrease and maintained 65.7% of its initial PL intensity value at 100 °C (Figure S6b). Remarkably, the decreased PL intensity can be fully recovered when the temperature was lowered to room temperature (∼25 °C) (Figure S6b). Moreover, UTS-QD@SiO_2 can be stable for a long period of time (*i.e.*, ∼7 days) at a temperature of 60 °C without a significant PL intensity decrease (less than 20% decrease, Figure S6d). In terms of photostability, UTS-QD@SiO_2 also showed an excellent performance with minimal PL intensity drop during a 7-day UV light (365 nm, 38 W) illumination (Figure S6c). Finally, we found that both the QD@SiO_2 samples in an aqueous phase exhibited good stabilities in all the commonly applied buffer solutions, including PBS, BS, Tris, and Hepes buffers (Figure S6e,f).

After stability tests of QD@SiO_2 in water, we further conjugated CRP2 antibodies to the surfaces of QD@SiO_2 through EDC coupling reactions (see the Experimental Section in the Supporting Information for details). PL spectra, dynamic light scattering (DLS), and zeta potential measurements of the final QD@SiO_2−antibody constructs were performed, and the results are shown in Figure 4. For UTS-QD@SiO_2−antibody probes, the PL spectra were symmetric and the peak positions did not change with varying the concentration of antibodies (Figure 4a). The fluorescence recovery (defined as the ratio of the measured PL intensity to the initial PL intensity during the recovery period) of those QDs can increase up to 90% (Table S2). However, TTS-QD@SiO_2−antibody can only keep above 80% (Figure S7a) due to the smaller size of the QDs that lead to loss of particles during the centrifugation process. As shown in Figure 4b, both the UTS-QD@SiO_2 and UTS-QD@SiO_2−antibody probes exhibited a narrow size distribution with a hydrodynamic size of 57.9 nm for UTS-QD@SiO_2. The hydrodynamic size of the final constructs gradually increased to 129.2 nm (1:1), 134.7 nm (1:2), 158.9 nm (1:4), and 179.9 nm (1:8) after conjugation with different amounts of CRP2 antibodies (Figure 4b and Table S2). The corresponding zeta potential changed from −46.1 mV to −32.3 mV (Figure 4c), being well within the range of stabilized colloids (>+30 mV or <−30 mV). Compared with UTS-QD@SiO_2, the hydrodynamic size of TTS-QD@SiO_2 increased from 57.9 to 135.3 nm when conjugating with an increased amount of CRP2 antibodies (UTS-QD@SiO_2:CRP2 = 1:1, 1:2, and 1:4). No further significant increases were observed at a UTS-QD@SiO_2:CRP2 ratio of 1:8 (Figure S7b). Both the TTS-QD@SiO_2 and the corresponding TTS-QD@SiO_2−antibody probes were colloidally stable with the measured zeta potentials of <−30 mV (Figure S7c). The PL QYs of 69% for UTS-QDs@SiO_2−antibody and 54% for TTS-QDs@SiO_2−antibody were obtained at optimal antibody coupling ratios. Compared to TTS-QD@SiO_2, each UTS-QD@SiO_2 can provide a larger average surface area (2.32×10^3 nm^2 *vs* 5.62×10^3 nm^2), which can offer more binding sites for antibody attachments. This improved antibody conjugation was confirmed by measuring the absorption spectrum of the supernatant solution during the EDC coupling process (Figure S8). The critical concentration of the antibodies that the QDs could couple to was determined *via* monitoring the intrinsic absorption peak of the antibody (∼280 nm). Before the measurement, the noise of the excess activating NHS reagent (also absorbs photons at a wavelength of 280 nm) was tentatively removed through four times centrifugal processes (see the details in the Supporting Information). The results showed that around 2-fold increased amounts of antibodies were conjugated to the UTS-QD@SiO_2 surfaces as compared to those of the TTS-QD@SiO_2 sample (Figure S8c,d).

Finally, we examined the performances of the UTS-QD@SiO_2−antibody and TTS-QD@SiO_2−antibody probes for CRP detection using a QDs-FLISA method (see details in the Experimental Section in the Supporting Information and Figure 5). Prior to the performance tests, the checkerboard titration experiment was designed to optimize the concentrations of coating CRP1 antibodies and QD−CRP2 antibody probes for the QDs-FLISA tests to achieve the best detecting

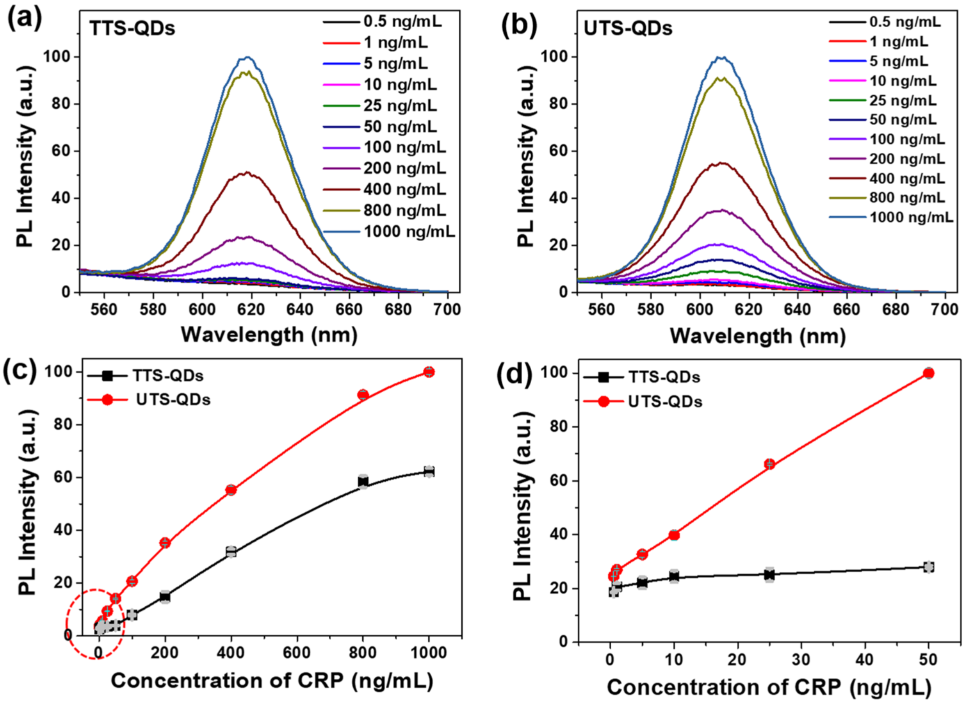

Figure 6. PL spectra from the QDs-FLISA method for determination of CRP antigens by TTS-QD@SiO_2−antibody (a) and UTS-QD@SiO_2−antibody (b). Corresponding calibration curves for CRP quantitative detection of 0−1000 ng/mL (c) and calibration curves at low concentration (0−50 ng/mL) of CRP antigens (d). Error bars indicate the standard deviations of three independent experiments.

Table 1. Comparison of Different Methods for CRP Detections Reported in the Literature

material	method	range (ng/mL)	LOD (ng/mL)	references
gold nanoparticles (GNPs)	GNP-based lateral flow immunoassay (LFIA)	50−450	50	61
streptavidin-conjugated horseradish peroxidase (SA-HRP)	ELISA	1−81	0.4	62
polystyrene beads	chemiluminescence assay	10−50,000	4	63
fluorescent nanospheres (FNs)	FN-based LFIA	25−1600	3.89	38
silica-encapsulated CdSe/ZnS	QDs-FLISA	1−1000	0.76	64
these UTS-QDs	UTS-QDs-FLISA	0.5−1000	0.41	this paper

performances (Table S3). The results showed that the optimal concentration for the coating antibody was 0.5 μg/well for CRP immunoassay and the diluting ratio of the QD−antibody probes was 1:100. The diluent buffer for the two types of QD@SiO_2−antibody probes was chosen as PBS containing 10% calf serum (v/v) according to the screening procedure (see the Supporting Information, Figure S8). The PL intensity of UTS-QD@SiO_2 systematically increased with increasing the concentration of antibodies up to 8-fold (Figure 5a). In contrast, the PL intensity of TTS-QD@SiO_2 was saturated after increasing the concentration of antibody to ∼4-fold (Figure 5b) due to the limited level of antibody conjugation. We then performed experiments on detecting different concentrations of the CRP antigen standard samples under the optimized conditions. The corresponding PL intensities were collected for each CRP sample at different CRP concentrations, and the results are plotted in Figure 6. Generally, the PL intensity gradually increased with increasing the concentration of CRP antigens for both the TTS-QD@SiO_2−antibody- and UTS-QD@SiO_2−antibody-based probes (Figure 6). Distinct behaviors for the two samples appeared at a low concentration regime of 0−50 ng/mL, where the UTS-QD@SiO_2 probes exhibited a high level of linear dependence of the PL intensity upon changing the CRP antigen concentration compared to the TTS-QD@SiO_2 probe (Figure 6d). The detection performances of these QD-based probes can be quantified by the limit of detection (LOD), an important parameter characterizing the antigen detection sensitivity in the QDs-FLISA method.[58,59] While the LOD was determined to be 1.12 ng/mL for the TTS-QD@SiO_2−antibody probes, the detection sensitivity was improved by around 2.7-fold to 0.41 ng/mL for the UTS-QD@SiO_2−antibody probes (see detailed LOD determination procedures in the Experimental Section). We also compared the CRP detection performances of the UTS-QD-based probes with other commercially available QDs obtained from different companies (Figure S16). The results showed that the UTS-QDs outperformed all other QD probes studied here by at least 2-fold enhancement in LOD under the same QDs-FLISA detection conditions (Figure S16). In addition, compared to other common methods, the UTS-QDs can serve as an efficient fluorescent probe for quantitative immunoassay with a wide detection range and a high detection sensitivity (Table 1).

To further evaluate the lifetime of the QD@SiO_2−antibody probes, we characterized the lifetimes of the QD@SiO_2−antibody probes by quantitatively monitoring the PL intensity changes while detecting high concentration of CRP antigens (1000 ng/mL) at two temperatures (*i.e.*, 4 and 45 °C) (see the Experimental Section in the Supporting Information for

https://dx.doi.org/10.1021/acsanm.0c03483
ACS Appl. Nano Mater. 2021, 4, 2855−2865

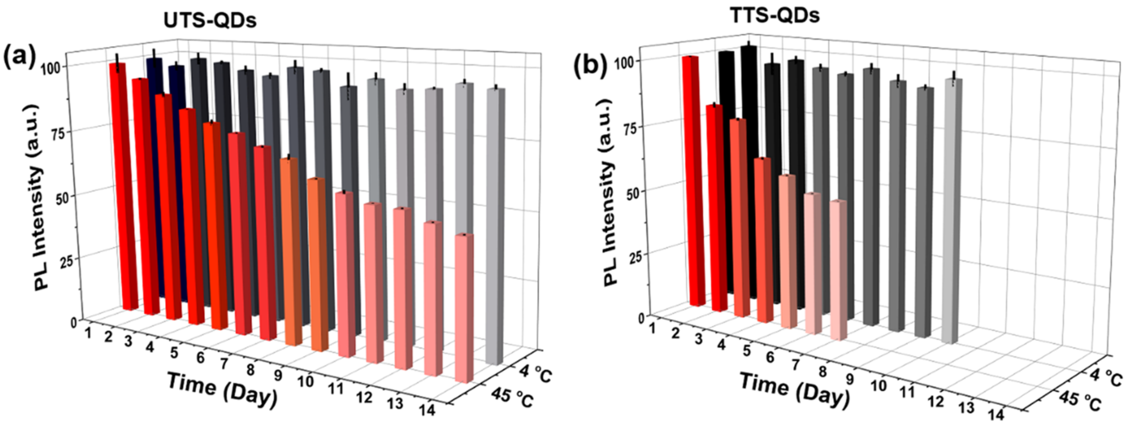

Figure 7. Evaluation lifetime of QDs-FLISA for CRP antigen detection of 1000 ng/mL by UTS-QD@SiO_2 (a) and TTS-QD@SiO_2 (b) at 4 °C (black column) and 45 °C (red column). Error bars indicate the standard deviations of three independent experiments.

details). To quantify the QD-based probe lifetime, we defined the T_{50} lifetime as the time within which the PL intensity of the QD-probe decays to 50% of its initial value.[60] For our UTS-QDs, the T_{50} lifetime of the probe was determined to be 14 days at 45 °C (Figure 7a, red bars), which was about two times longer than that of the TTS-QD-based probe (∼7 days, Figure 7b, red bars). As expected, both types of QD−antibody probes demonstrated excellent stability with minimal PL intensity variations at ∼4 °C for at least 10 days (Figure 7, black bars). The stability evaluations of QDs-FLISA at medium (100 ng/mL) and low concentrations (10 ng/mL) were also provided (see Figure S10 in the Supporting Information). In addition, we noted that the T_{50} lifetimes (at 45 °C) of all the commercial QDs tested here were around 7 days, which were comparable to those of the TTS-QDs and dramatically shorter than those of the UTS-QD-based probes (Figure S17). Furthermore, to validate the practical application of QDs-FLISA for CRP, the recoveries of the spiked samples were determined by detecting different concentrations of CRP in human serum samples, including the low-, medium-, and high-risk levels. As shown in Table 2, the recoveries of the QDs-FLISA method using UTS-QD- and TTS-QD-based probes were from 97.5% to 110.0% with a relative standard deviation (RDS) of less than 10%. These results demonstrated the potential of the QDs-FLISA method using UTS-QDs in future clinical applications.

Table 2. Recoveries of Different Concentrations of CRP Antigen in Human Negative Serum

material	sample number (n = 5)	spiked value (ng/mL)	real value (ng/mL)	recovery (%)	RDS (%)
UTS-QDs	1	10	10.5	105.0	7.30
	2	100	99.7	99.7	3.44
	3	800	780.1	97.5	8.11
TTS-QDs	1	10	11.0	110.0	8.15
	2	100	104.4	104.4	4.60
	3	800	782.2	97.8	9.98

3. CONCLUSIONS

In conclusion, we have successfully synthesized UTS CdSe/ZnS/CdZnS/ZnS core/shell QDs with high PL QYs of above 80% and suppressed single-QD blinking through a long-term shell growth at a high reaction temperature (≥310 °C). Compared to the TTS CdSe/CdS/ZnS core/shell QDs, the newly synthesized UTS-QDs exhibited superior optical properties at both ensemble and single-dot levels and improved pH, thermal, and photostabilities with more robust optical performance against phase transferring from organic to aqueous solution. Moreover, we have applied the UTS-QDs for CRP antigen detection following a QDs-FLISA procedure. Compared to the TTS-QDs and four different commercially available core/shell QDs, a nearly 3-fold enhancement in the detection sensitivity was observed when utilizing the UTS-QD-based antibody probes. The LOD value reached as low as 0.41 ng/mL, and the probe lifetime showed at least a 2-fold increment. Compared to other common detection methods, the use of UTS-QDs as a fluorescent probe for quantitative immunoassay offers a wide detection range and a high detection sensitivity with a superior detection accuracy. Our study presented here demonstrates a colloidal synthesis of a new type of high-quality QDs, which can serve as stable and efficient bio-detection materials. We believe that our discovery will generate broad interest and be of great technological importance for high-sensitivity and high-accuracy protein detections in the field of bio-labeling, sensing, and detection.

■ ASSOCIATED CONTENT

Supporting Information

The Supporting Information is available free of charge at https://pubs.acs.org/doi/10.1021/acsanm.0c03483.

Energy level diagram, UV−vis absorption, PL spectra, lifetimes, and XPS of Cd 3d, Zn 2p, and S 2p for UTS-QDs and TTS-QDs (Figures S1−S4); HAADF-STEM image of TTS-QDs (Figure S5); stability data of UTS-QD@SiO_2 and TTS-QD@SiO_2 (Figure S6); QD−antibody information (Figures S7 and S8 and Tables S1 and S2); characterization of the screening process and stability evaluation of QDs-FLISA (Figures S9 and S10 and Table S3); and characterization of commercially available core/shell QDs (Figures S11−S17) (PDF)

■ AUTHOR INFORMATION

Corresponding Authors

Dangdang Xu − *Key Laboratory for Special Functional Materials of Ministry of Education, School of Materials and Engineering, Henan University, Kaifeng 475004, China*; Email: ddxu@henu.edu.cn

Ou Chen − *Department of Chemistry, Brown University, Providence, Rhode Island 02912, United States;* orcid.org/0000-0003-0551-090X; Email: ouchen@brown.edu

Lin Song Li − *Key Laboratory for Special Functional Materials of Ministry of Education, School of Materials and Engineering, Henan University, Kaifeng 475004, China;* orcid.org/0000-0001-7015-3211; Email: lsli@henu.edu.cn

Authors

Yanbing Lv − *Key Laboratory for Special Functional Materials of Ministry of Education, School of Materials and Engineering, Henan University, Kaifeng 475004, China*

Yucheng Yuan − *Department of Chemistry, Brown University, Providence, Rhode Island 02912, United States;* orcid.org/0000-0003-3935-0967

Ning Hu − *Key Laboratory for Special Functional Materials of Ministry of Education, School of Materials and Engineering, Henan University, Kaifeng 475004, China*

Na Jin − *Department of Chemistry, Brown University, Providence, Rhode Island 02912, United States*

Ruili Wu − *Key Laboratory for Special Functional Materials of Ministry of Education, School of Materials and Engineering, Henan University, Kaifeng 475004, China;* orcid.org/0000-0002-6667-5903

Huaibin Shen − *Key Laboratory for Special Functional Materials of Ministry of Education, School of Materials and Engineering, Henan University, Kaifeng 475004, China;* orcid.org/0000-0002-6425-0514

Complete contact information is available at:
https://pubs.acs.org/10.1021/acsanm.0c03483

Author Contributions

The manuscript was written through contributions of all authors. All authors have given approval to the final version of the manuscript.

Notes

The authors declare no competing financial interest.

■ ACKNOWLEDGMENTS

The authors gratefully acknowledge the financial support from the National Natural Science Foundation of China (grant nos. 61922028, 61874039, 21671058, 81902158, and 21905074).

■ REFERENCES

(1) Medintz, I. L.; Uyeda, H. T.; Goldman, E. R.; Mattoussi, H. Quantum Dot Bioconjugates for Imaging, Labelling and Sensing. *Nat. Mater.* **2005**, *4*, 435−446.

(2) Smith, A. M.; Mancini, M. C.; Nie, S. Second Window for in Vivo Imaging. *Nat. Nanotechnol.* **2009**, *4*, 710−711.

(3) Ca, N. X.; Lien, V. T. K.; Nghia, N. X.; Chi, T. T. K.; Phan, T. L. Type-II CdS/ZnSe Core/Shell Heterostructures: UV−vis Absorption, Photoluminescence and Raman Scattering Studies. *Mater. Sci. Eng., B* **2015**, *200*, 107−116.

(4) Bruns, O. T.; Bischof, T. S.; Harris, D. K.; Franke, D.; Shi, Y.; Riedemann, L.; Bartelt, A.; Jaworski, F. B.; Carr, J. A.; Rowlands, C. J.; Wilson, M. W. B.; Chen, O.; Wei, H.; Hwang, G. W.; Montana, D. M.; Coropceanu, I.; Achorn, O. B.; Kloepper, J.; Heeren, J.; So, P. T. C.; Fukumura, D.; Jensen, K. F.; Jain, R. K.; Bawendi, M. G. Next-generation in Vivo Optical Imaging with Short-wave Infrared Quantum Dots. *Nat. Biomed. Eng.* **2017**, *1*, 0056.

(5) Michalet, X.; Pinaud, F. F.; Bentolila, L. A.; Tsay, J. M.; Doose, S.; Li, J. J.; Sundaresan, G.; Wu, A. M.; Gambhir, S. S.; Weiss, S. Quantum Dots for Live Cells, in Vivo Imaging, and Diagnostics. *Science* **2005**, *307*, 538−544.

(6) Heine, M.; Fischer, A. W.; Schlein, C.; Jung, C.; Straub, L. G.; Gottschling, K.; Mangels, N.; Yuan, Y.; Nilsson, S. K.; Liebscher, G.; Chen, O.; Schreiber, R.; Zechner, R.; Scheja, L.; Heeren, J. Lipolysis Triggers a Systemic Insulin Response Essential for Efficient Energy Replenishment of Activated Brown Adipose Tissue in Mice. *Cell Metab.* **2018**, *28*, 644−655.e4.

(7) Ma, Y.; Mao, G.; Huang, W.; Wu, G.; Yin, W.; Ji, X.; Deng, Z.; Cai, Z.; Zhang, X.-E.; He, Z.; Cui, Z. Quantum Dot Nanobeacons for Single RNA Labeling and Imaging. *J. Am. Chem. Soc.* **2019**, *141*, 13454−13458.

(8) Saif, M.; Kwanten, W. J.; Carr, J. A.; Chen, I. X.; Posada, J. M.; Srivastava, A.; Zhang, J.; Zheng, Y.; Pinter, M.; Chatterjee, S.; Softic, S.; Kahn, C. R.; Van Leyen, K.; Bruns, O. T.; Jain, R. K.; Bawendi, M. G. Non-invasive Monitoring of Chronic Liver Disease via Near-infrared and Shortwave-infrared Imaging of Endogenous Lipofuscin. *Nat. Biomed. Eng.* **2020**, *4*, 801−813.

(9) Dahan, M.; Laurence, T.; Pinaud, F.; Chemla, D. S.; Alivisatos, A. P.; Sauer, M.; Weiss, S. Time-gated Biological Imaging by Use of Colloidal Quantum Dots. *Opt. Lett.* **2001**, *26*, 825−827.

(10) Fu, A.; Gu, W.; Boussert, B.; Koski, K.; Gerion, D.; Manna, L.; Le Gros, M.; Larabell, C. A.; Alivisatos, A. P. Semiconductor Quantum Rods as Single Molecule Fluorescent Biological Labels. *Nano Lett.* **2007**, *7*, 179−182.

(11) Jing, L.; Ding, K.; Kershaw, S. V.; Kempson, I. M.; Rogach, A. L.; Gao, M. Magnetically Engineered Semiconductor Quantum Dots as Multimodal Imaging Probes. *Adv. Mater.* **2014**, *26*, 6367−6386.

(12) Franke, D.; Harris, D. K.; Chen, O.; Bruns, O. T.; Carr, J. A.; Wilson, M. W. B.; Bawendi, M. G. Continuous Injection Synthesis of Indium Arsenide Quantum Dots Emissive in the Short-wavelength Infrared. *Nat. Commun.* **2016**, *7*, 12749.

(13) Gao, X.; Cui, Y.; Levenson, R. M.; Chung, L. W. K.; Nie, S. In Vivo Cancer Targeting and Imaging with Semiconductor Quantum Dots. *Nat. Biotechnol.* **2004**, *22*, 969−976.

(14) McNamara, J. O., II; Andrechek, E. R.; Wang, Y.; Viles, K. D.; Rempel, R. E.; Gilboa, E.; Sullenger, B. A.; Giangrande, P. H. Cell Type-specific Delivery of siRNAs with Aptamer-siRNA Chimeras. *Nat. Biotechnol.* **2006**, *24*, 1005−1015.

(15) Han, M.; Gao, X.; Su, J. Z.; Nie, S. Quantum-dot-tagged Microbeads for Multiplexed Optical Coding of Biomolecules. *Nat. Biotechnol.* **2001**, *19*, 631−635.

(16) Choi, Y.; Kim, H. P.; Hong, S. M.; Ryu, J. Y.; Han, S. J.; Song, R. In Situ Visualization of Gene Expression Using Polymer-coated Quantum-dot-DNA Conjugates. *Small* **2009**, *5*, 2085−2091.

(17) Gill, R.; Zayats, M.; Willner, I. Semiconductor Quantum Dots for Bioanalysis. *Angew. Chem., Int. Ed.* **2008**, *47*, 7602−7625.

(18) Chen, H.; Crum, M.; Chavan, D.; Vu, B.; Kourentzi, K.; Willson, R. C. Nanoparticle-based Proximity Ligation Assay for Ultrasensitive, Quantitative Detection of Protein Biomarkers. *ACS Appl. Mater. Interfaces* **2018**, *10*, 31845−31849.

(19) Jin, Z.; Hildebrandt, N. Semiconductor Quantum Dots for In Vitro Diagnostics and Cellular Imaging. *Trends Biotechnol.* **2012**, *30*, 394−403.

(20) Goldman, E. R.; Anderson, G. P.; Tran, P. T.; Mattoussi, H.; Charles, P. T.; Mauro, J. M. Conjugation of Luminescent Quantum Dots with Antibodies Using an Engineered Adaptor Protein to Provide New Reagents for Fluoroimmunoassays. *Anal. Chem.* **2002**, *74*, 841−847.

(21) Zrazhevskiy, P.; Sena, M.; Gao, X. Designing Multifunctional Quantum Dots for Bioimaging, Detection, and Drug delivery. *Chem. Soc. Rev.* **2010**, *39*, 4326−4354.

(22) Chauhan, V. P.; Popović, Z.; Chen, O.; Cui, J.; Fukumura, D.; Bawendi, M. G.; Jain, R. K. Fluorescent Nanorods and Nanospheres for Real-Time in Vivo Probing of Nanoparticle Shape-Dependent Tumor Penetration. *Angew. Chem., Int. Ed.* **2011**, *50*, 11417−11420.

(23) Chen, O.; Riedemann, L.; Etoc, F.; Herrmann, H.; Coppey, M.; Barch, M.; Farrar, C. T.; Zhao, J.; Bruns, O. T.; Wei, H.; Guo, P.; Cui, J.; Jensen, R.; Chen, Y.; Harris, D. K.; Cordero, J. M.; Wang, Z.;

Jasanoff, A.; Fukumura, D.; Reimer, R.; Dahan, M.; Jain, R. K.; Bawendi, M. G. Magneto-fluorescent Core-shell Supernanoparticles. *Nat. Commun.* **2014**, *5*, 5093.

(24) Baker, S. N.; Baker, G. A. Luminescent Carbon Nanodots: Emergent Nanolights. *Angew. Chem., Int. Ed.* **2010**, *49*, 6726−6744.

(25) Gnaim, S.; Green, O.; Shabat, D. The Emergence of Aqueous Chemiluminescence: New Promising Class of Phenoxy 1,2-dioxetane Luminophores. *Chem. Commun.* **2018**, *54*, 2073−2085.

(26) Wegner, K. D.; Hildebrandt, N. Quantum Dots: Bright and Versatile in vitro and in vivo Fluorescence Imaging Biosensors. *Chem. Soc. Rev.* **2015**, *44*, 4792−4834.

(27) Huang, L.; Wu, Q.; Wang, J.; Foda, M.; Liu, J.; Cai, K.; Han, H. A Brilliant Sandwich Type Fluorescent Nanostructure Incorporating a Compact Quantum Dot Layer and Versatile Silica Substrates. *Chem. Commun.* **2014**, *50*, 2896−2899.

(28) Huang, L.; Liao, T.; Wang, J.; Ao, L.; Su, W.; Hu, J. Brilliant Pitaya-Type Silica Colloids with Central−Radial and High-Density Quantum Dots Incorporation for Ultrasensitive Fluorescence Immunoassays. *Adv. Funct. Mater.* **2018**, *28*, 1705380.

(29) Jeong, S.; Achermann, M.; Nanda, J.; Ivanov, S.; Klimov, V. I.; Hollingsworth, J. A. Effect of the Thiol-Thiolate Equilibrium on the Photophysical Properties of Aqueous CdSe/ZnS Nanocrystal Quantum Dots. *J. Am. Chem. Soc.* **2005**, *127*, 10126−10127.

(30) Yu, W. W. Semiconductor Quantum Dots: Synthesis and Water-Solubilization for Biomedical Applications. *Expert Opin. Biol. Ther.* **2008**, *8*, 1571−1581.

(31) Chu, X.; Dou, X.; Liang, R.; Li, M.; Kong, W.; Yang, X.; Luo, J.; Yang, M.; Zhao, M. A Self-assembly Aptasensor Based on Thick-shell Quantum Dots for Sensing of Ochratoxin A. *Nanoscale* **2016**, *8*, 4127−4133.

(32) Yuan, Y.; Zhu, H.; Wang, X.; Cui, D.; Gao, Z.; Su, D.; Zhao, J.; Chen, O. Cu-Catalyzed Synthesis of CdZnSe-CdZnS Alloy Quantum Dots with Highly Tunable Emission. *Chem. Mater.* **2019**, *31*, 2635−2643.

(33) García-Santamaría, F.; Chen, Y.; Vela, J.; Schaller, R. D.; Hollingsworth, J. A.; Klimov, V. I. Suppressed Auger Recombination in "Giant" Nanocrystals Boosts Optical Gain Performance. *Nano Lett.* **2009**, *9*, 3482−3488.

(34) Chen, O.; Zhao, J.; Chauhan, V. P.; Cui, J.; Wong, C.; Harris, D. K.; Wei, H.; Han, H.-S.; Fukumura, D.; Jain, R. K.; Bawendi, M. G. Compact High-quality CdSe-CdS Core-shell Nanocrystals with Narrow Emission Linewidths and Suppressed Blinking. *Nat. Mater.* **2013**, *12*, 445−451.

(35) Bae, W. K.; Park, Y.-S.; Lim, J.; Lee, D.; Padilha, L. A.; McDaniel, H.; Robel, I.; Lee, C.; Pietryga, J. M.; Klimov, V. I. Controlling the Influence of Auger Recombination on the Performance of Quantum-dot Light-emitting Diodes. *Nat. Commun.* **2013**, *4*, 2661.

(36) Tan, R.; Yuan, Y.; Nagaoka, Y.; Eggert, D.; Wang, X.; Thota, S.; Guo, P.; Yang, H.; Zhao, J.; Chen, O. Monodisperse Hexagonal Pyramidal and Bipyramidal Wurtzite CdSe-CdS Core-Shell Nanocrystals. *Chem. Mater.* **2017**, *29*, 4097−4108.

(37) Li, J.; Lv, Y.; Li, N.; Wu, R.; Xing, M.; Shen, H.; Li, L. S.; Chen, X. Robust Synthesis of Bright Multiple Quantum Dot-embedded Nanobeads and Its Application to Quantitative Immunoassay. *Chem. Eng. J.* **2019**, *361*, 499−507.

(38) Hu, J.; Zhang, Z.-L.; Wen, C.-Y.; Tang, M.; Wu, L.-L.; Liu, C.; Zhu, L.; Pang, D.-W. Sensitive and Quantitative Detection of C-reaction Protein Based on Immunofluorescent Nanospheres Coupled with Lateral Flow Test Strip. *Anal. Chem.* **2016**, *88*, 6577−6584.

(39) Li, J. J.; Wang, Y. A.; Guo, W.; Keay, J. C.; Mishima, T. D.; Johnson, M. B.; Peng, X. Large-Scale Synthesis of Nearly Monodisperse CdSe/CdS Core/Shell Nanocrystals Using Air-Stable Reagents via Successive Ion Layer Adsorption and Reaction. *J. Am. Chem. Soc.* **2003**, *125*, 12567−12575.

(40) Ca, N. X.; Lien, V. T. K.; Nghia, N. X.; Chi, T. T. K.; Phan, T.-L. Tunable Luminescent Emission Characterization of Type-I and Type-II Systems in CdS-ZnSe Core-Shell Nanoparticles: Raman and Photoluminescence Study. *Nanotechnology* **2015**, *26*, 445701.

(41) Ca, N. X.; Hien, N. T.; Tan, P. M.; Phan, T. L.; Thanh, L. D.; Do, P. V.; Bau, N. Q.; Lien, V. T. K.; Van, H. T. Tunable Dual Emission in Type-I/Type-II CdSe/CdS/ZnSe Nanocrystals. *J. Alloys Compd.* **2019**, *791*, 144−151.

(42) Shen, H.; Lin, Q.; Wang, H.; Qian, L.; Yang, Y.; Titov, A.; Hyvonen, J.; Zheng, Y.; Li, L. S. Efficient and Bright Colloidal Quantum Dot Light-Emitting Diodes via Controlling the Shell Thickness of Quantum Dots. *ACS Appl. Mater. Interfaces* **2013**, *5*, 12011−12016.

(43) Shen, H.; Lin, Q.; Cao, W.; Yang, C.; Shewmon, N. T.; Wang, H.; Niu, J.; Li, L. S.; Xue, J. Efficient and Long-lifetime Full-color Light-emitting Diodes Using High Luminescence Quantum Yield Thick-shell Quantum Dots. *Nanoscale* **2017**, *9*, 13583−13591.

(44) Dabbousi, B. O.; Rodriguez-Viejo, J.; Mikulec, F. V.; Heine, J. R.; Mattoussi, H.; Ober, R.; Jensen, K. F.; Bawendi, M. G. (CdSe)ZnS Core-Shell Quantum Dots: Synthesis and Characterization of a Size Series of Highly Luminescent Nanocrystallites. *J. Phys. Chem. B* **1997**, *101*, 9463−9475.

(45) Qin, H.; Niu, Y.; Meng, R.; Lin, X.; Lai, R.; Fang, W.; Peng, X. Single-Dot Spectroscopy of Zinc-Blende CdSe/CdS Core/Shell Nanocrystals: Nonblinking and Correlation with Ensemble Measurements. *J. Am. Chem. Soc.* **2014**, *136*, 179−187.

(46) Mahler, B.; Lequeux, N.; Dubertret, B. Ligand-controlled Polytypism of Thick-shell CdSe/CdS Nanocrystals. *J. Am. Chem. Soc.* **2010**, *132*, 953−959.

(47) Chen, O.; Yang, Y.; Wang, T.; Wu, H.; Niu, C.; Yang, J.; Cao, Y. C. Surface-Functionalization-Dependent Optical Properties of II-VI Semiconductor Nanocrystals. *J. Am. Chem. Soc.* **2011**, *133*, 17504−17512.

(48) Chen, O.; Wei, H.; Maurice, A.; Bawendi, M.; Reiss, P. Pure Colors from Core-shell Quantum Dots. *MRS Bull.* **2013**, *38*, 696−702.

(49) Li, M.; Li, X.; An, X.; Chen, Z.; Xiao, H. Clustering-Triggered Emission of Carboxymethylated Nanocellulose. *Front. Chem.* **2019**, *7*, 447.

(50) Shen, H.; Wang, H.; Chen, X.; Niu, J. Z.; Xu, W.; Li, X. M.; Jiang, X.-D.; Du, Z.; Li, L. S. Size- and Shape-Controlled Synthesis of CdTe and PbTe Nanocrystals Using Tellurium Dioxide as the Tellurium Precursor. *Chem. Mater.* **2010**, *22*, 4756−4761.

(51) Zhu, H.; Fan, Z.; Yu, L.; Wilson, M. A.; Nagaoka, Y.; Eggert, D.; Cao, C.; Liu, Y.; Wei, Z.; Wang, X.; He, J.; Zhao, J.; Li, R.; Wang, Z.; Grünwald, M.; Chen, O. Controlling Nanoparticle Orientations in the Self-Assembly of Patchy Quantum Dot-Gold Heterostructural Nanocrystals. *J. Am. Chem. Soc.* **2019**, *141*, 6013−6021.

(52) Nirmal, M.; Dabbousi, B. O.; Bawendi, M. G.; Macklin, J. J.; Trautman, J. K.; Harris, T. D.; Brus, L. E. Fluorescence Intermittency in Single Cadmium Selenide Nanocrystals. *Nature* **1996**, *383*, 802−804.

(53) Zhang, H.; Wang, F.; Kuang, Y.; Li, Z.; Lin, Q.; Shen, H.; Wang, H.; Guo, L.; Li, L. S. Se/S Ratio-Dependent Properties and Application of Gradient-Alloyed $CdSe_{1-x}S_x$ Quantum Dots: Shell-free Structure, Non-blinking Photoluminescence with Single-Exponential Decay, and Efficient QLEDs. *ACS Appl. Mater. Interfaces* **2019**, *11*, 6238−6247.

(54) Chen, Y.; Vela, J.; Htoon, H.; Casson, J. L.; Werder, D. J.; Bussian, D. A.; Klimov, V. I.; Hollingsworth, J. A. "Giant" Multishell CdSe Nanocrystal Quantum Dots with Suppressed Blinking. *J. Am. Chem. Soc.* **2008**, *130*, 5026−5027.

(55) Wang, X.; Ren, X.; Kahen, K.; Hahn, M. A.; Rajeswaran, M.; Maccagnano-Zacher, S.; Silcox, J.; Cragg, G. E.; Efros, A. L.; Krauss, T. D. Non-blinking Semiconductor Nanocrystals. *Nature* **2009**, *459*, 686−689.

(56) Koole, R.; van Schooneveld, M. M.; Hilhorst, J.; de Mello Donegá, C.; Hart, D. C.; van Blaaderen, A.; Vanmaekelbergh, D.; Meijerink, A. On the Incorporation Mechanism of Hydrophobic Quantum Dots in Silica Spheres by a Reverse Microemulsion Method. *Chem. Mater.* **2008**, *20*, 2503−2512.

(57) Acebrón, M.; Galisteo-López, J. F.; Granados, D.; López-Ogalla, J.; Gallego, J. M.; Otero, R.; López, C.; Juárez, B. H. Protective

Ligand Shells for Luminescent SiO_2-Coated Alloyed Semiconductor Nanocrystals. *ACS Appl. Mater. Interfaces* **2015**, *7*, 6935−6945.

(58) Armbruster, D. A.; Pry, T. Limit of Blank, Limit of Detection and Limit of Quantitation. *Clin. Biochem. Rev.* **2008**, *29*, S49−S52.

(59) Xu, D.-D.; Deng, Y.-L.; Li, C.-Y.; Lin, Y.; Tang, H.-W. Metal-Enhanced Fluorescent Dye-Doped Silica Nanoparticles and Magnetic Separation: A Sensitive Platform for One-Step Fluorescence Detection of Prostate Specific Antigen. *Biosens. Bioelectron.* **2017**, *87*, 881−887.

(60) Song, J.; Wang, O.; Shen, H.; Lin, Q.; Li, Z.; Wang, L.; Zhang, X.; Li, L. S. Over 30% External Quantum Efficiency Light-Emitting Diodes by Engineering Quantum Dot-Assisted Energy Level Match for Hole Transport Layer. *Adv. Funct. Mater.* **2019**, *29*, 1808377.

(61) Raj, V.; Sreenivasan, K. Selective Detection and Estimation of C-reactive Protein in Serum Using Surface-Functionalized Gold Nano-particles. *Anal. Chim. Acta* **2010**, *662*, 186−192.

(62) Ridker, P. M. Clinical Application of C-reactive Protein for Cardiovascular Disease Detection and Prevention. *Circulation* **2003**, *107*, 363−369.

(63) Vashist, S. K.; Czilwik, G.; van Oordt, T.; von Stetten, F.; Zengerle, R.; Marion Schneider, E.; Luong, J. H. T. One-step Kinetics-based Immunoassay for the Highly Sensitive Detection of C-reactive Protein in Less Than 30 min. *Anal. Biochem.* **2014**, *456*, 32−37.

(64) Lv, Y.; Li, J.; Wu, R.; Wang, G.; Wu, M.; Shen, H.; Li, L. S. Silica-encapsulated Quantum Dots for Highly Efficient and Stable Fluorescence Immunoassay of C-reactive Protein. *Biochem. Eng. J.* **2018**, *137*, 344−351.